



OPEN

Development and application of similar material for physical model test of an ultradeep foundation pit in round gravel strata

Yanhui Guo¹✉, Xipeng Ren¹, Shaoqian Liu¹, Xiaobing Fu², Guo Yuan², Guoyang Zhang², Yi Yang¹, Zhiqian Yang¹, Xiangyu Wang² & Ming Ni²

The raw-material mix ratio and preparation of similar materials are crucial for the success of physical model tests and for accurately reflecting prototype properties. In this study, an optimum similar material for plateau alluvial and lacustrine (PAL) round gravel was developed based on similarity theory. The similar materials were subjected to sensitivity factor analysis and microscopic analysis. Subsequently, the optimum similar material was applied to a three-dimensional (3D) physical model test of an ultradeep foundation pit (FP). The findings show that the similar material prepared with gypsum, LD, bentonite, water, barite powder, and DS at a ratio of 1:1:1.4:3.5:8.8:13.2 was the best for a 3D physical model test of the ultradeep FP in PAL round gravel strata. The sensitivity-factor analysis revealed that barite powder had the greatest impact on γ , that c and ϕ were primarily affected by bentonite, and that the LD-gypsum ratio controlled E . A nonuniform particle-size distribution as well as the presence of “edge-to-face” contacts and small pores between particles constituted the microphysical factors affecting the mechanical properties of the optimum similar material. Using dolomite with a Mohs hardness of 3.5–4 instead of traditional quartz sand with a Mohs hardness of 7 as the raw material can produce a similar material for the target soil with mechanical parameters closer to those of the ideal similar material. The application of the optimum similar material in physical model tests has revealed the stress field response law of ultra deep foundation pit excavation. This study could provide reference and inspiration for the development of similar materials in gravel formations with weaker mechanical properties.

Keywords Plateau alluvial and lacustrine round gravel, Similar material, Sensitivity-factor analysis, Microscopic analysis, Three-dimensional physical model test, Ultradeep foundation pit

As the limited urban surface space can no longer meet the growing demands of everyday life, the urban underground space is being developed vigorously and at an increasing scale^{1–3}. Consequently, a series of engineering problems has emerged, such as large foundation pit (FP) excavation depths and coverage areas, complex geological conditions, and a dramatic increase in construction and support difficulties^{4–6}. In geotechnical engineering, physical model tests are generally conducted to solve problems that would otherwise require labor- and resource-intensive and time-consuming field tests. This approach also eschews errors caused by the simplification of geotechnical structures in theoretical calculations and numerical simulation methods^{7,8}. In addition, physical model test results can provide a reference for the construction of complex FPs in the field.

The raw-material mix ratio and preparation of similar materials are deciding factors for the success of physical model tests and provide a basis for physical model tests to accurately reflect prototype properties in the field^{9–11}. Numerous researchers have extensively studied and contributed to the development of similar materials for rock and soil masses. Li Hang et al.¹² simulated the soft soil layer in Shanghai by using silty clay, barite powder, bentonite, laundry powder, EPE pearl cotton foam and water, and studied the deformation trend of the enclosure and adjacent tunnels during the excavation of foundation pit based on these materials. Wang et al.⁹ developed a new similar material for geo mechanical model tests, termed iron–barite–sand–cemented material, which consists of a mixture of iron concentrate powder, barite powder, QS, gypsum, rosin, and an alcohol solution. By

¹Faculty of Public Safety and Emergency Management, Kunming University of Science and Technology, Kunming 650093, China. ²Yunnan Construction Investment No. 6 Construction Co., Ltd., Yuxi 653199, China. ✉email: guoyanhui0818@kust.edu.cn

orthogonal design and regression analysis, Peng et al.¹³ obtained the optimal ratio of new transparent similar materials suitable for tunnel surrounding rock by using fused quartz sand, nano-scale white carbon black and n-dodecane mixed 15# white oil as raw materials. Fan et al.¹⁴ determined the raw-material mix ratio for a similar material and its relationship with mechanical metrics through a minimum number of orthogonal and additional local tests. Using the orthogonal design method, Yonghua et al.¹⁵ adopted orthogonal design and used fine sand, coarse sand, cement and gypsum as raw materials to determine the similar material ratio suitable for soft rock as follows: fine sand: coarse sand: cement: gypsum = 12:18:5:5. Jongpradist et al.¹⁶ experimentally investigated fracture initiation and propagation directions in rock masses using 200 scaled-down artificial rock samples at various stress ratios, overburden stresses, and joint dip angles. Wang et al.¹⁷ used cement, alpha high-strength gypsum, quartz sand, barite powder and water as raw materials supplemented by polycarboxylic acid water-reducing agent, defoamer and retarding agent, etc., to develop a composite material with similar brittleness and rock-burst tendency index to on-site granite. Miao et al.¹⁸ formulated a similar material for shaking table model tests with bentonite, clay, silty fine sand, and barite powder as raw materials and performed a sensitivity analysis of each mix factor affecting the physical and mechanical parameters of the similar material. Based on the orthogonal test (OT) design method, Dou et al.¹⁹ experimentally investigated the raw-material mix ratios used to prepare similar materials for soft soils with barite powder, QS, gypsum, bentonite, laundry detergent (LD), and water as raw materials; they also analyzed the sensitivity of each factor using the extreme difference analysis method, and studied the effects of each factor on similar material parameters. Wang et al.²⁰ examined the mechanical properties and acoustic emission response patterns of similar materials for sand and paraffin prepared at different mix ratios to reveal the deformation, stress, and fracture patterns of coal and rock and their dynamic disaster evolution mechanism. Wang et al.²¹ determined the effects of the raw-material mix ratio on the mechanical properties of a similar material for soft soils through direct shear, unconfined compressive strength, and laboratory triaxial tests, as well as analyzed its micromorphological characteristics through scanning electron microscopy (SEM). Chu et al.²² developed a new rheological similar material to simulate soft rock and investigated the effects of each component on its instantaneous elastic-plastic parameters and Burger's model rheological parameters through OTs. Fu et al.²³ developed similar materials for silty mudstone with low strength and expansibility upon hydration using conventional materials such as gypsum, barite powder, clay minerals, and distilled water at a mix ratio determined based on the orthogonal design method. With the cement-to-water ratio, cement-to-sand ratio, and QS particle size as control factors, Yang et al.²⁴ used QS, 42.5 ordinary Portland cement, and water as raw materials to prepare a material with similar properties to those of conglomerate. Xu et al.²⁵ developed similar materials for tunnel surrounding rocks with elastic modulus, uniaxial compressive strength, and density as keymetrics; they also analyzed the effects of the raw-material composition on the key metrics and applied the results to a physical model test of tunnel lining cracks. Based on the similarity principle of geomechanical model tests, Guo et al.²⁶ developed new coupled liquid-solid similar materials for faults and surrounding rocks suitable for water and mud inrush model tests with mountain sand, red clay, cement, and water through a large number of proportioning tests.

With the efforts of numerous scholars both domestically and internationally, similar materials developed based on different geological conditions have been gradually applied in physical model tests of foundation pit engineering, and certain research results have been achieved. Using barite powder, iron ore powder, quartz sand, liquid paraffin, rosin, gypsum powder and water as raw materials, Zhang et al.²⁷ prepared similar materials suitable for the foundation pit of Shenzhen Metro station through orthogonal design, and tested their physical and mechanical properties. The results showed that the similar materials could truly reflect the change of earth pressure during excavation. Based on large-scale (1:10) physical model tests using soil similar materials, Dou et al.²⁸ found that the data on the passive earth pressure obtained from the experiments were basically consistent with field observations in terms of both their magnitude and the trend of variations in them with the depth of excavation. Mu et al.²⁹ took the Luoyang Railway Station subway station open pit support project as a background and conducted three groups of small-scale model tests on the lateral displacement change law of the support structure during pit excavation. They explored the displacement change law of the pit support piles after the excavation of the pit and considered the influence of different pile spacing. Yang²⁴ studied the deformation mechanism of pit excavation, the impact on adjacent buildings, etc. with the background of Chongqing Shapingba Railway Hub oversized deep foundation pit project, after preparing similar materials using large-scale indoor model test methods³⁰.

Despite their rapid progress, most research mainly focuses on clay, silt, sandy soil, and expansive soil and loess as special soils, except for the PAL round gravel. The gravelly soil consists of large, round particles, and has a high water content and high permeability. These properties posed several challenges to the construction of the pit, including the poor quality of the pile, easily collapsible holes, and inrushing water into the holes of the anchor cables. Further in-depth research on similar materials for the PAL round gravel is urgently required. In addition, most 3D physical model tests involving similar materials are performed to examine tunnels, mines, and slopes. However, the situation surrounding the construction of FPs has become increasingly dire, urgently requiring an investigation of ultradeep FPs based on 3D physical model tests. Hence, based on previous studies, we developed a similar material that has a simple composition and can be easily fabricated to simulate PAL round gravel, and applied it to a 3D physical model test of an ultradeep FP.

Overview of an ultradeep FP project in PAL round gravel strata

The No. 14 Kunming water purification plant construction project involves the construction of a fully buried underground sewage treatment plant in the Panlong district of Kunming in Yunnan Province, China, which is situated at approximately 1981 m above sea level in the center of the Yunnan–Guizhou Plateau. The project is divided into four sections of construction. The present experimental study examined the influent pump

Soil layer no.	Name	Specific weight γ /(kN/m ³)	Cohesion c /(kPa)	Internal friction angle φ /(°)	Compression modulus E_s /(MPa)
③	Round gravel	22.2	7.4	31.9	26.0
③2	Silt	18.9	37.2	15.2	8.9
④	Round gravel	22.2	7.4	31.9	26.0
④1	Clay	18.1	39.4	9.3	9.0
④2	Silt	19.5	29.0	8.0	12.3
⑤	Round gravel	22.2	7.4	31.9	26.0
⑥	Round gravel	22.2	7.4	31.9	26.0

Table 1. Quaternary alluvial and lacustrine strata in the lower part of the site and their mechanical metrics.



Fig. 1. Project site photo.

station in the first section, featuring an earth volume of 22,400 m³, a design depth of 33 m, a plane area of 32 m (length) × 25 m (width), a FP with a perimeter length of 114 m.

The construction of the entire FP supports follows the principle of starting with the deepest and most difficult area and progressing towards the shallowest and easiest area. The elevation relative to the ground surface at the end of the excavation of the ultradeep FP of the influent pump station is -33 m. The support structure consists of slurry walls and five layers of reinforced-concrete internal supports. The slurry wall is 1.2 m in thickness and is constructed to a depth of 44 m. The strength grade of the concrete is C35. Each reinforced-concrete internal support has a cubic shape with a side length of 1.2 m.

As revealed by drilling data, the lithology of the strata where the FP is to be constructed consists primarily of Quaternary alluvial and lacustrine gravel, sand, clayey soil, silt, and peat. Due to the paleo-Dianchi Lake Basin and the sedimentary environment of the Panlong River within the basin, a thick layer of alluvial and lacustrine round gravel has accumulated in the northern urban area of Kunming. The surface stratum of the site predominantly comprises miscellaneous fill (layer ①) and silty clay (layer ②). The lower part of the site is dominated by round gravel. The round gravel layers are generally interconnected. The Quaternary alluvial and lacustrine round gravel layers mainly consist of layers ③, ④, ⑤, and ⑥. Within the excavation depth of the FP, most of the unit layers in layers ①–⑤ at the site will be exposed. The rare Quaternary alluvial and lacustrine round gravel strata in the plateau region constitute the primary object of excavation during the construction of the ultradeep FP of the influent pump station and the surrounding soil affected during the excavation and support. When excavating the ultra-deep foundation pit in gravel strata that are both aquifers and permeable layers, the support method of "internal support and slurry walls" is adopted with strong anti-seepage performance, large wall stiffness, and small engineering disturbance and deformation. When the groundwater level changes or too much water accumulates in the pit due to the thicker gravel layer and changes in natural precipitation, the site adopts compaction grouting measures to fill up the ground, and increases the number of wells to control the groundwater level. Table 1 summarizes the Quaternary alluvial and lacustrine strata in the lower part of the site and their mechanical metrics. Figures 1 and 2 show the photo of site photo and round gravel soil sampling point.

Determination of similarity constants

In a physical model test, the field prototype is scaled down according to a certain ratio based on similarity theory, followed by the construction of a physical model using a similar material made from a variety of raw materials. Subsequently, a physical process is applied to the physical model, and its mechanical behavior and deformation pattern are observed. A physical model must strictly satisfy the similarity theory that links it to the prototype. Specifically, the similarity theory involves geometric, material, and physical-process similarity^{31–35}.

Considering the spatial conditions of indoor experiments and the possibility of losing model details due to excessive geometric similarity constants, $C_l = 100$ was chosen. To ensure the similarity of dynamic characteristics and shear behavior between the model and the prototype, C_γ and $C_\varphi = 1$ were chosen. In addition, the similarity constant of dimensionless physical quantities



Fig. 2. Photo of round gravel soil sampling point.

Physical quantity	Similarity theory	Prototype	Similarity constants	Model
Dimensional metrics	$C_l = \frac{l_P}{l_M}$	32 m*25 m*33 m	$Cl=100$	32 cm*25 cm*33 cm
Specific weight	$C_\gamma = \frac{\gamma_P}{\gamma_M}$	22.2 kN/m ³	$C\gamma=1$	22.2 kN/m ³
Cohesion Internal friction angle	$C\tau = \frac{\tau_P}{\tau_M} = \frac{cP + \sigma P \tan \varphi P}{cM + \sigma M \tan \varphi M}$	7.4 kPa 31.9°	$C_c=10$ $C\varphi=1$	0.74 kPa 31.9°
Poisson's ratio	$Cv = \frac{v_P}{v_M} = \frac{\varepsilon x(P)/\varepsilon y(P)}{\varepsilon x(M)/\varepsilon y(M)}$	0.46	$Cv=1$	0.46
Compression modulus	$C_E = \frac{E_P}{E_M} = \frac{\sigma P/\varepsilon P}{\sigma M/\varepsilon M} = \frac{C\sigma}{C\varepsilon}$	26 MPa	$CE=10$	2.6 MPa

Table 2. summarizes the mechanical metrics of the ideal similar material for PAL round gravel.

$$C_\varepsilon = C_v = 1 \quad (1)$$

From the definite formula (2) and the inference (3)

$$G = E/2(1 + \nu) \quad (2)$$

$$2(1 + \nu) = E_P/G_P = C_E E_M/C_G/G_M \quad (3)$$

we can obtain

$$C_G = C_E \quad (4)$$

Similarly, from the definite formula

$$E = \sigma/\varepsilon \quad (5)$$

we can derive

$$C_E = C_\sigma \quad (6)$$

In physical model tests, the use of the identicale similar constants for mechanical and geometrical physical quantities is usually defective in a generalized sense. Therefore, the cohesion similarity constant $C_c = 10$ is corrected to avoid similar materials infinitely close to the bulk state, with reference to the study of Yu Yifan. When $C_c = 10$ and $C_\varphi = 1$, $C_\tau = C_\sigma = 10$ according to Coulomb's law

$$\tau = c + \sigma \tan \varphi \quad (7)$$

In summary,

$$C_G = C_E = C_\sigma = C_\tau = C_c \quad (8)$$

Generally, P, M, and C are used to denote the prototype, the model, and the similarity constants between the physical quantities of the prototype and the model, respectively. Table 2 summarizes the mechanical metrics of the ideal similar material for PAL round gravel.



Fig. 3. Raw materials used to prepare the similar material.

Material name	Characteristic	Main components	Mesh	Specific weight γ /(kN/m ³)
Dolomite sand	Yellow particles	Dolomite, muscovite	20~140	16
Barite powder	Grey powder	$\text{BaSO}_4 > 90\%$	325	45
Bentonite	Milky powder	Sodium luminosilicate	325	25
Gypsum	White powder	$\text{CaSO}_4 > 93\%$	—	23
Laundry detergent	Blue viscous liquid	Surfactant, softener	—	12

Table 3. Parameters of the raw materials comprising the similar material.

Similar material development

Selection of raw materials

Select the raw materials in Fig. 3 to prepare similar materials: dolomite sand (DS) and barite powder (aggregate); gypsum and LD (binder); and bentonite (additive). DS is a low γ , low c , and high φ material, and barite powder is a high γ and low c material, and the two, as the main components of similar materials, can effectively mimic the high γ and high φ of PAL gravel soil but at the same time keep the c at a low level. Therefore, high c gypsum and LD were chosen as the binder. As the main active ingredient of LD, nonionic surfactants can reduce the water tension and fine tune the c of the similar material.

As the main component of the binder, The gypsum reacted with water to form the gypsum dihydrate ($\text{CaSO}_4 \cdot 2\text{H}_2\text{O}$). It forms a crystal grid structure that enhances the bonding between the particles, therefoer, increasing the proportion of gypsum may increase the c of similar materials. On the contrary, increasing the proportion of LD may decrease the c of similar materials. Because the non-ionic surfactant in LD (the main component is "surfactant, softener") will reduce the surface tension of water, reduce the capillary force between particles, weaken the viscosity of the binder, resulting in a decrease in the bond strength between particles, and reduce the effective contact area and weaken the cementing ability of gypsum. The bentonite has volume expansion and viscosity under the presence of water. The more its content, the lower γ and the higher c of similar materials. Controlling the aggregate–binder ratio, the LD–gypsum ratio in the binder material, and the barite powder, bentonite, and water content can allow the mechanical properties of the similar material to fluctuate randomly within a certain range that covers the mechanical parameters of the ideal similar material. Table 3 summarizes the parameters of the raw materials comprising the similar material.

OT scheme design

OTs conducted based on an orthogonal table are uniformly dispersed and regularly comparable³⁶. This approach allows for an optimal ratio for a similar material to be determined through a small number of tests. An orthogonal table ensures that each level of each factor is paired once with each level of each of the remaining factors. This is also the most suitable experimental design method for similar material development.

Referring to the process of Dou¹⁹ orthogonal experiment, this paper adopts aggregate: binder = 11:1 to basically determine the random range of each factor level. Referring to the OT design idea of Liu et al³⁷, the horizontal random range is divided by equidistant distance. Four influencing factors were designed, including washing paste ratio, barite powder, bentonite and water content, and three levels were set for each factor. A total of 9 groups of tests were carried out³⁸. The scale Table 4 was prepared as follows, and $L_9(3^4)$ OT table of similar material ratio schemes was obtained, as shown in Table 5.

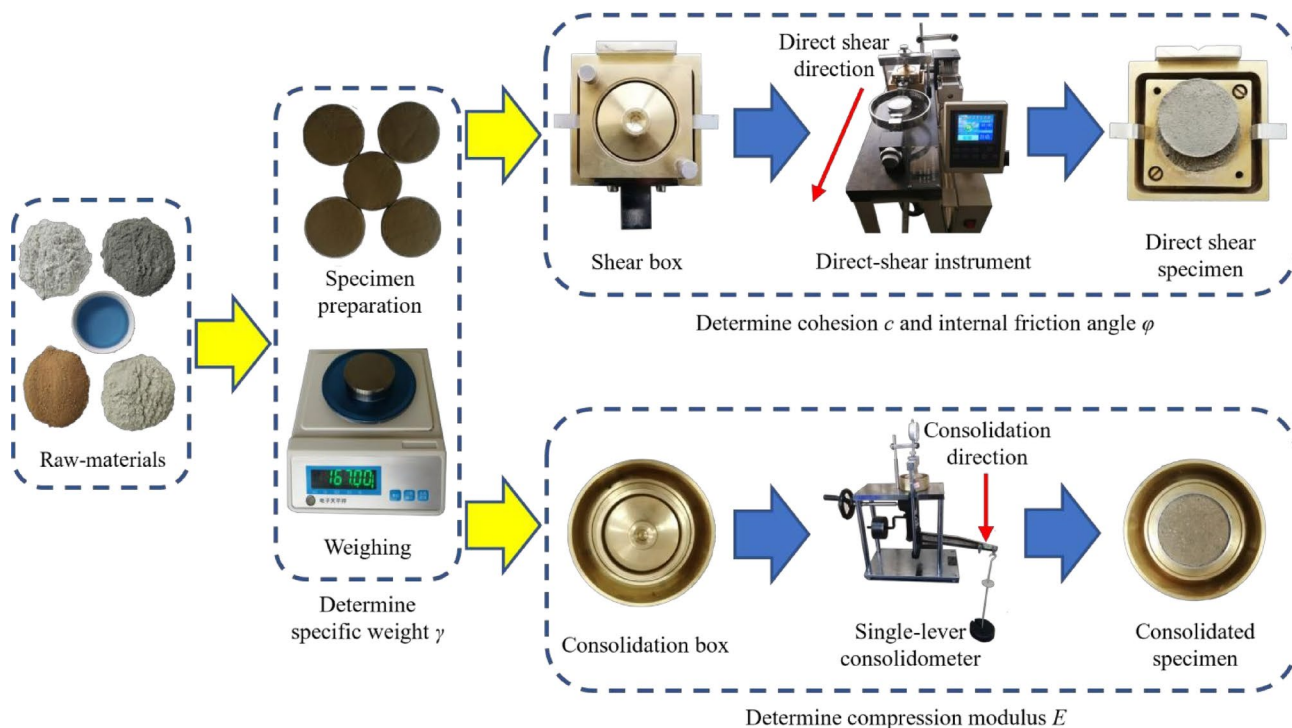
Determination of the key control metrics

The nine similar materials composed of the raw materials that were obtained based on the OT design were subjected to weighing, direct shear, and consolidation tests to determine the key control metrics, namely, γ , c , φ , and E . To facilitate this, specimens were prepared as follows: DS, barite powder, gypsum powder, and bentonite were added successively based on their proportions in each similar material. The mixture was then stirred well and injected with LD and water, followed by further stirring until the raw materials were well mixed and devoid

Factors	Level 1	Level 2	Level 3
LD-gypsum ratio	4:6	5:5	6:4
Barite powder	20	30	40
Bentonite	5	10	15
Water content	8	12	16

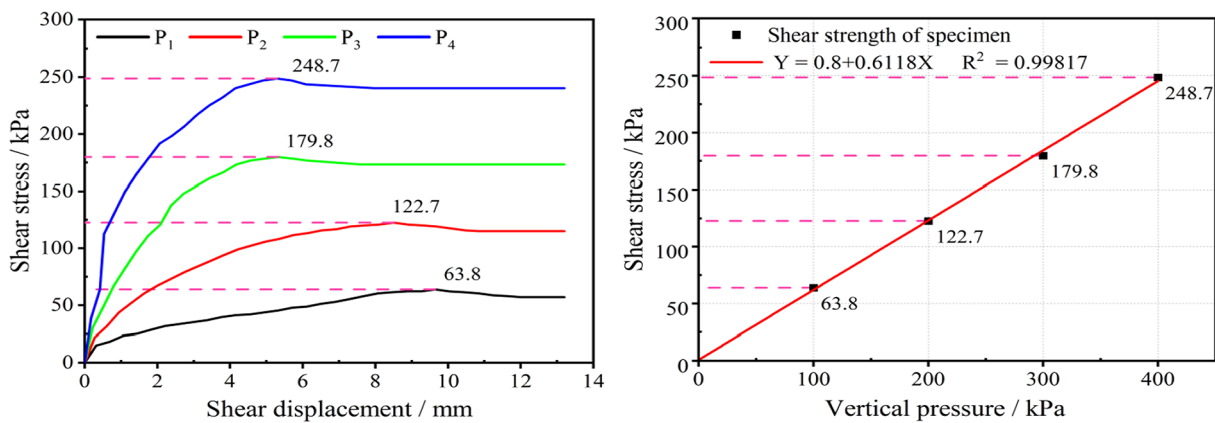
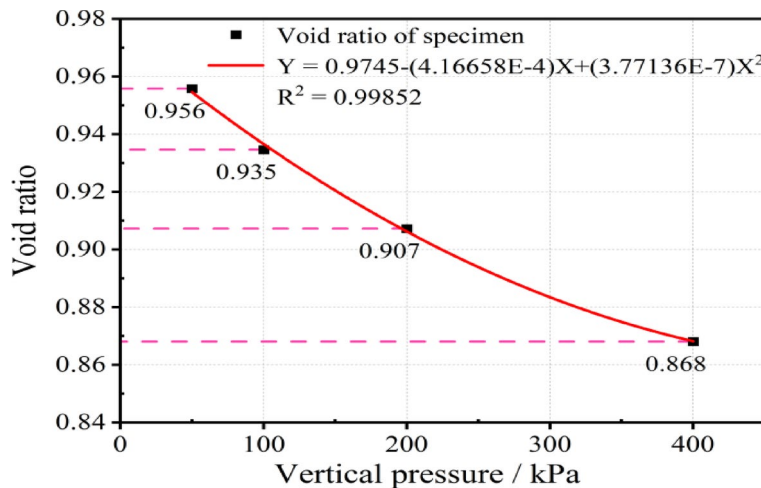
Table 4. Level design for each factor in the OT.

Test No	Factors			
	LD-gypsum ratio	Barite powder (%)	Bentonite (%)	Water content (%)
1	4:6	20	5	8
2	4:6	30	10	12
3	4:6	40	15	16
4	5:5	20	10	16
5	5:5	30	15	8
6	5:5	40	5	12
7	6:4	20	15	12
8	6:4	30	5	16
9	6:4	40	10	8

Table 5. $L_9(3^4)$ OT table for the proportioning scheme for the similar materials.**Fig. 4.** Specimen preparation and parameter determination workflow.

of clots. Each prepared similar material specimen was loaded into a ring knife and then compacted, after which both sides of the ring knife were leveled using a geotechnical knife. After each specimen was prepared, γ was first determined based on the fixed volume of the ring knife and the weight measurement of the specimen. Next, the specimen was subjected to direct shear and consolidation tests to determine its c , ϕ , and E . Figure 4 shows the specimen preparation and parameter determination workflow.

For each similar material, four specimens were sheared at a rate of 0.8 mm/min under vertical pressures of 100, 200, 300, and 400 kPa, respectively, to failure within 3–5 min. A curve of shear stress versus shear displacement is calculated for each specimen based on equally spaced force gauge readings. The specimen is damaged in shear

Fig. 5. A typical p - τ curve (6#).Fig. 6. A typical p - e relationship (6#).

when the force gauge needle no longer advances or recedes significantly. The c and ϕ of each similar material were obtained by processing the test data using the Mohr–Coulomb equation. Figure 5 shows a typical p - τ curve. Where, X represents the stress applied to the specimen in the vertical direction, and Y represents the shear strength of the specimen under different stress conditions.

E was measured through rapid consolidation tests. Four specimens were compressed at 50, 100, 200, and 400 kPa for 1 h. At 400 kPa, deformation was measured at both 1 and 24 h. The deformation at each previous level of pressure was corrected based on that at 400 kPa. Calculate the porosity ratio based on the unit settlement, and the coefficient of compression and E were further calculated. Figure 6 shows a typical p - e relationship. Where, X represents the vertical pressure applied to the sample, and Y represents the pore ratio of the sample under different pressures.

Figure 7 and Table 6 show the OT results for the similar material proportioning test, that is the mechanical metrics for the nine similar materials (No. 1–9) and the ideal similar material (No. 10). Where, the horizontal coordinate is the number of groups in the orthogonal experiment, and the vertical coordinate is the value of corresponding parameters of similar materials. The mechanical metrics of the ideal similar material were used as a reference for the best similar material, termed the optimum similar material. A comprehensive analysis of all the key control metrics clearly revealed that the No. 6 similar material (y : 22.7 kN/m³; c : 0.8 kPa; ϕ : 35°; E : 3.91 MPa) was closer to the ideal similar material. Therefore, the No. 6 similar material was selected as the optimum similar material for PAL round gravel strata and was applied to a 3D physical model test of the ultradeep FP. A conversion yielded the following original raw-material mix ratio for the optimum similar material: gypsum: LD: bentonite: water: barite powder: DS = 1: 1: 1.4: 3.5: 8.8: 13.2.

Sensitivity factor analysis

The key control metrics of the similar material were subjected to a sensitivity factor analysis using the extreme-difference calculation method in OT theory. The extreme difference reflects the impact of different levels of the influencing factor on the metric. A large extreme difference suggests that different levels of the factor led to a

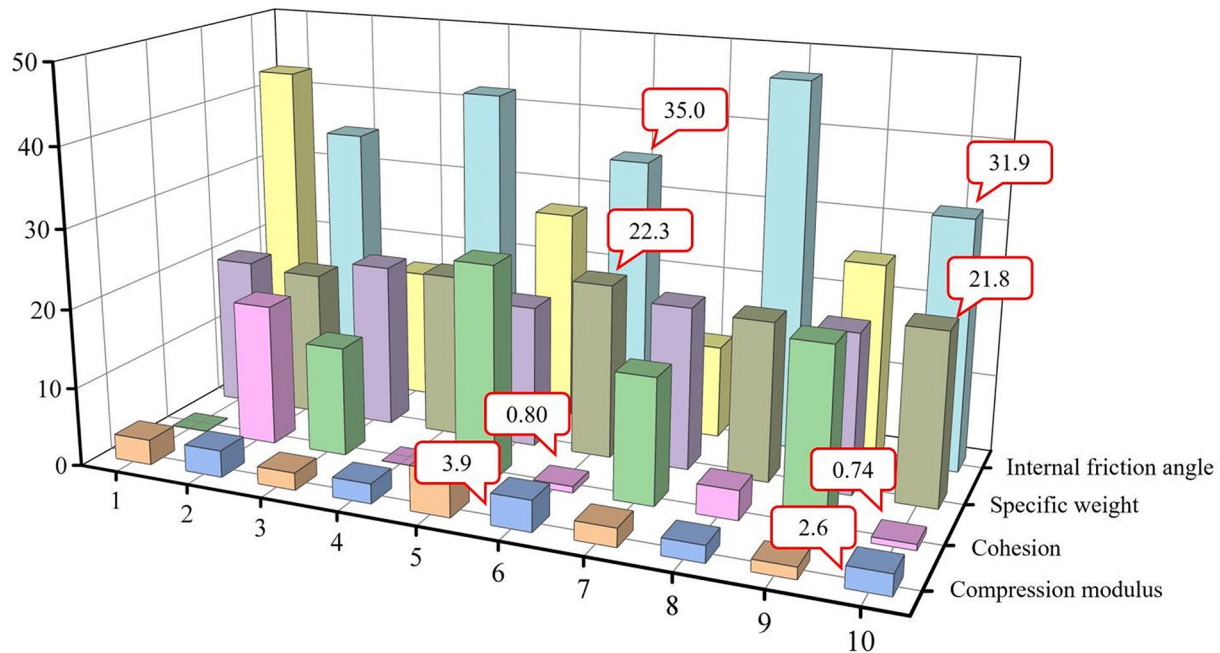


Fig. 7. The OT results for the similar material proportioning test.

Experiment number	Density (g/cm ³)	Cohesion c(kPa)	internal friction angle ϕ (°)	Compression modulus E(MPa)
1	1.97	0	42.7	3.18
2	1.91	18	35	3.38
3	2.14	13.9	16.8	2.18
4	2.13	0	42	2.49
5	1.85	26.9	27.1	5.63
6	2.23	0.8	35	3.91
7	2.11	15.9	11.9	2.33
8	2.06	3.7	46.9	2.11
9	2.06	22.6	25.1	1.46
10	2.18	0.74	31.9	2.6

Table 6. Proportional Test Plan Based on Orthogonal Design.

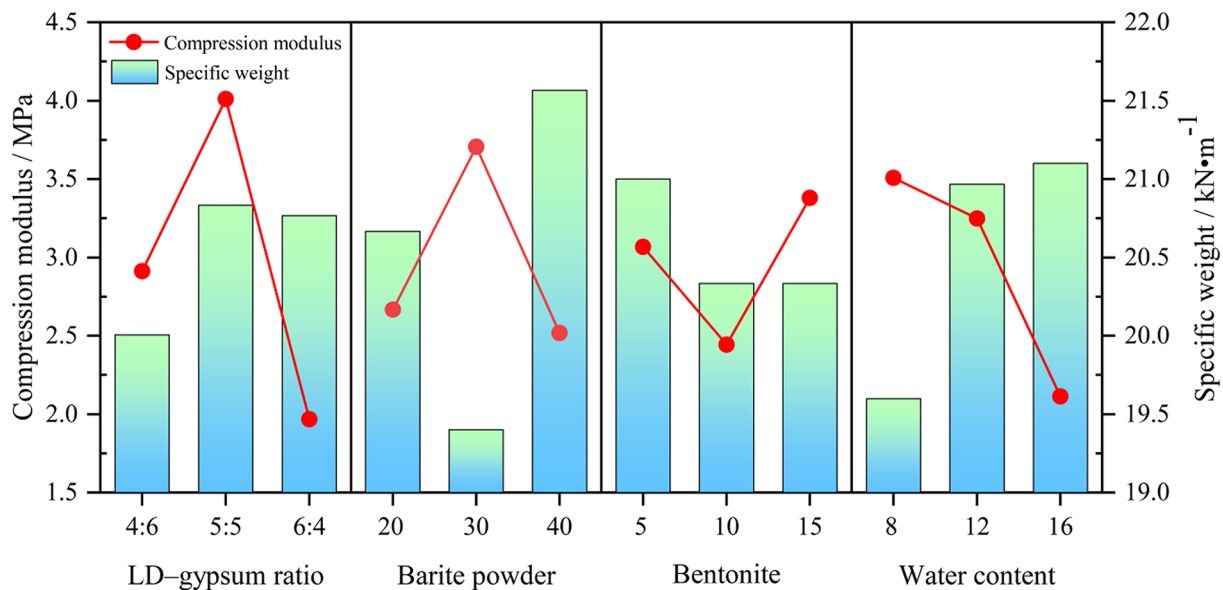
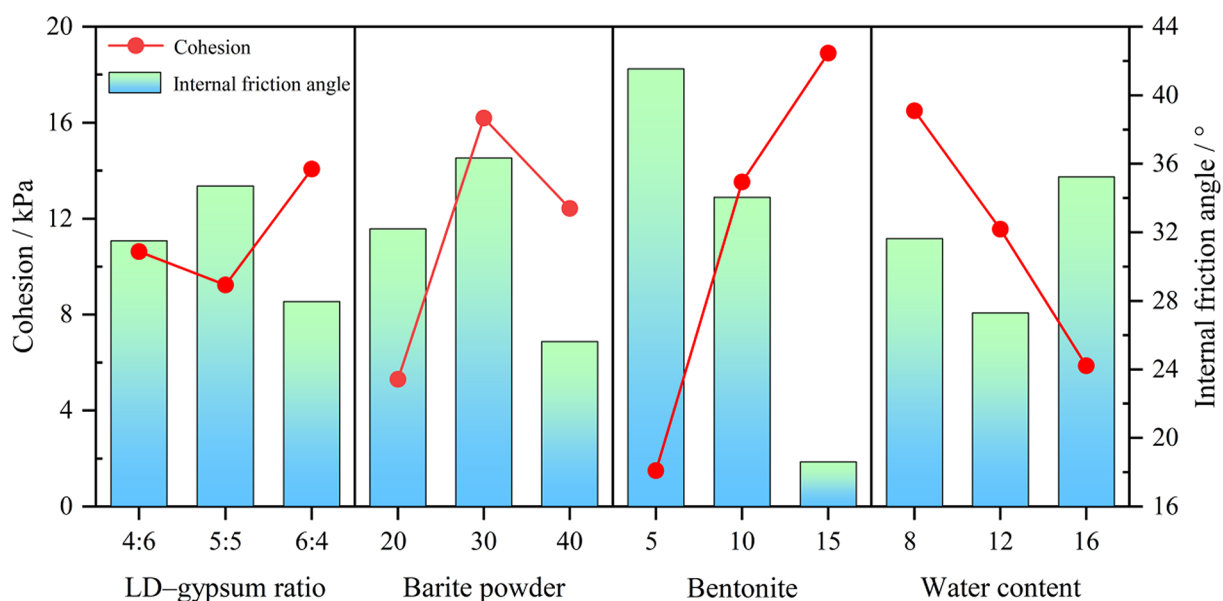
significant difference in test results and is a sensitivity factor affecting the key control metric. To obtain a visual understanding, the sensitivity of each factor to each key control metric was plotted. Figure 8 shows the sensitivity factors for E and γ , and Fig. 9 shows the sensitivity factors for c and ϕ .

Figures 8 and 9 shows that an increase in the water content led to an increase in γ and a decrease in both c and E. An increase in the bentonite content resulted in an increase in c and a decrease in both γ and ϕ . No significant linear relationships were evident between the remaining factors and each key control metric. In addition, the small number of controls prevented the identification and analysis of peak values. According to the range values of key control indicators, the E of similar materials decreases steeply from 4.01 to 1.96 MPa when the LD–gypsum ratio is adjusted from 5:5 to 6:4, and the γ of similar materials increases from 19.40 to 21.56 kN/m³ when the barite powder is adjusted from 30 to 40%. Analyzing the most sensitive factors for each key control indicator, it was found that the most sensitive factor for E is the LD–gypsum ratio, the most sensitive factor for γ is the content of barite powder, while the most sensitive factors for c and ϕ are the content of bentonite.

Microscopic analysis of the optimum similar material

Morphological analysis

In this study, a VEGA-3SBH tungsten-filament SEM system (Tescan, Czech Republic) was used to observe the microscopic characteristics of the best similar material to evaluate its mechanical properties. Block specimens with structural integrity and continuity facilitated the observation of connection patterns and porosity between units. Powdered specimens that have been lightly ground without destroying the basic units facilitate the observation of morphological features and particle size distribution. Therefore, four specimens (two powder and two block) of optimally similar materials were prepared in order to obtain homogeneous and reliable

Fig. 8. Sensitivity factors for E and γ .Fig. 9. Sensitivity factors for c and φ .

observations. The observation followed the principle of first finding scanning points at a low magnification and then observing the scanning points at a high magnification. In addition, based on the particle size of the optimum similar material, an appropriate magnification factor was selected to obtain a suitable observation field of view^{39,40}.

The microstructure of the optimum similar material in powder form was mainly analyzed to determine its particle size. Under the microscope, the powder specimens of the optimum similar material appeared to comprise largely inseparable aggregates with strong original c as well as a large number of dispersed particles (e.g., flakes and grains) with low roundness.

Based on the statistical results of particle distribution, the particles were highly nonuniform and unfilled. Superfine particles ($< 1.0 \mu\text{m}$) accounted for 5.4%, agglomerates ($> 10 \mu\text{m}$) accounted for 6.7%, and particles ($1.0\text{--}5.0 \mu\text{m}$) and fine particles ($5.0\text{--}10.0 \mu\text{m}$) together accounted for 87.83%. A total of 74 particle size samples were collected in Sample 1, with a mean particle size of $3.94 \mu\text{m}$ and a minimum particle size of $0.8 \mu\text{m}$. The largest particle size collected from Sample 1 was $16.67 \mu\text{m}$, but agglomerates with larger particle sizes can be observed in Sample 2 and can be basically determined to be dolomitic sand. Figure 10 shows the SEM images of the optimum similar material in powder form.

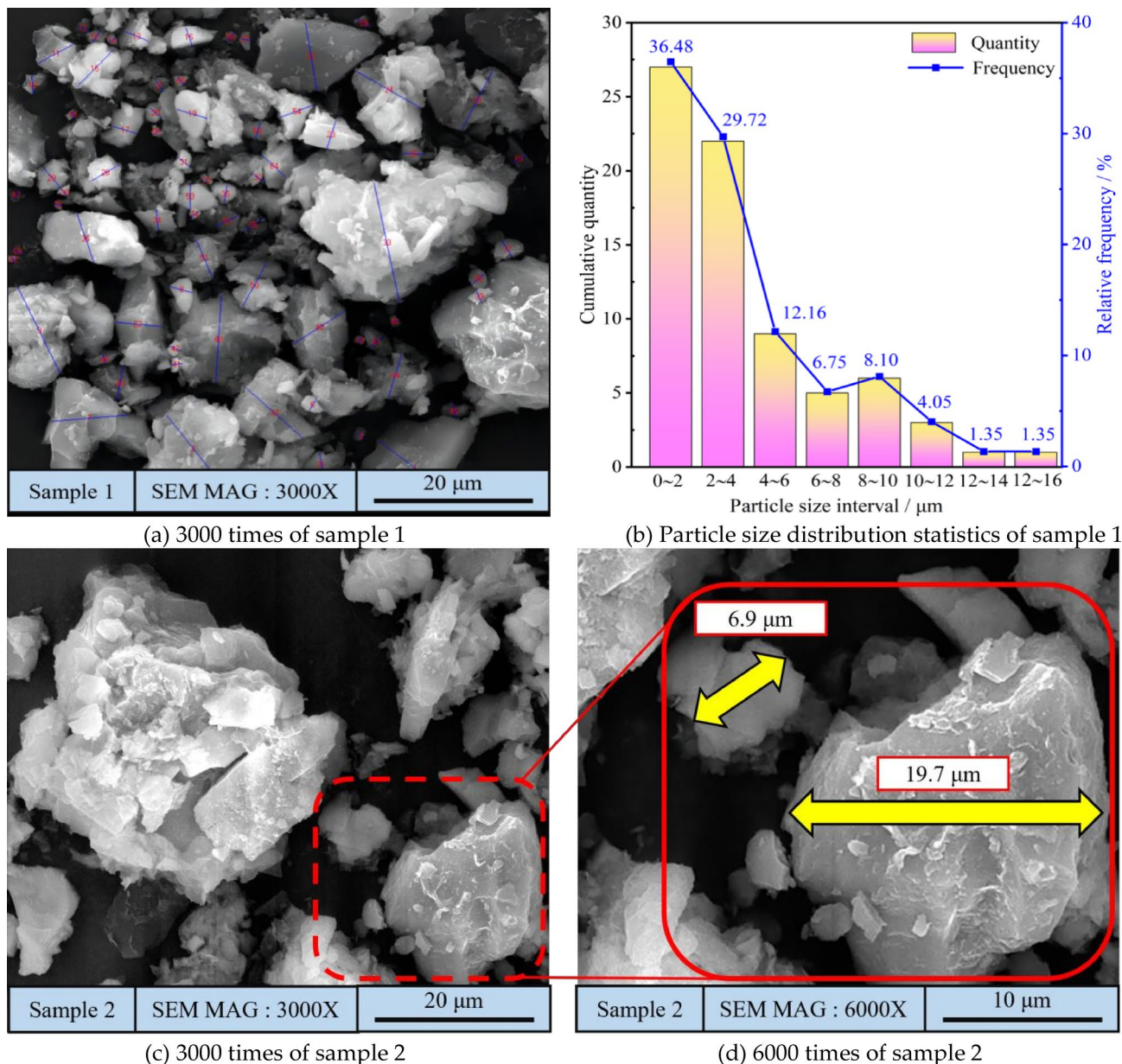


Fig. 10. The SEM images of the optimum similar material in powder form.

The microstructure of the similar material in block form was analyzed mainly for the modes of contact and pore characteristics. Most soil skeleton particles in the similar material were agglomerated and clotted. Skeleton connections consisted mostly of edge-to-face and face-to-face contacts, with few edge-to-edge contacts. In addition, the soil skeleton appeared to comprise concentrated flakes or plates. The fine particles composing the gypsum and bentonite—two materials that become viscous in the presence of water—were adhered to areas other than the skeleton. The two block samples exhibited essentially similar pore distribution patterns: the pores were nonuniformly distributed and consisted of a large number of small pores (typically varying from 1 to 3 μm in size) and a small number of large pores (typically varying from 10 to 20 μm in size). Figure 11 shows the SEM images of the optimum similar material in block form.

An observation of the particle size, contact modes, and pore characteristics of the powder and block specimens of the optimum similar material revealed three major causes of the low c and low E of the optimum similar material: nonuniform particle-size distribution, edge-to-face contacts and a small number of edge-to-edge contacts between particles, and small pores and a small number of large pores between particles. A careful observation of the contact modes between the small particles in the block specimens preliminarily suggested that the LD and water content induced reduction in the viscosity of the gypsum and bentonite was a cause of the low c of the optimum similar material.

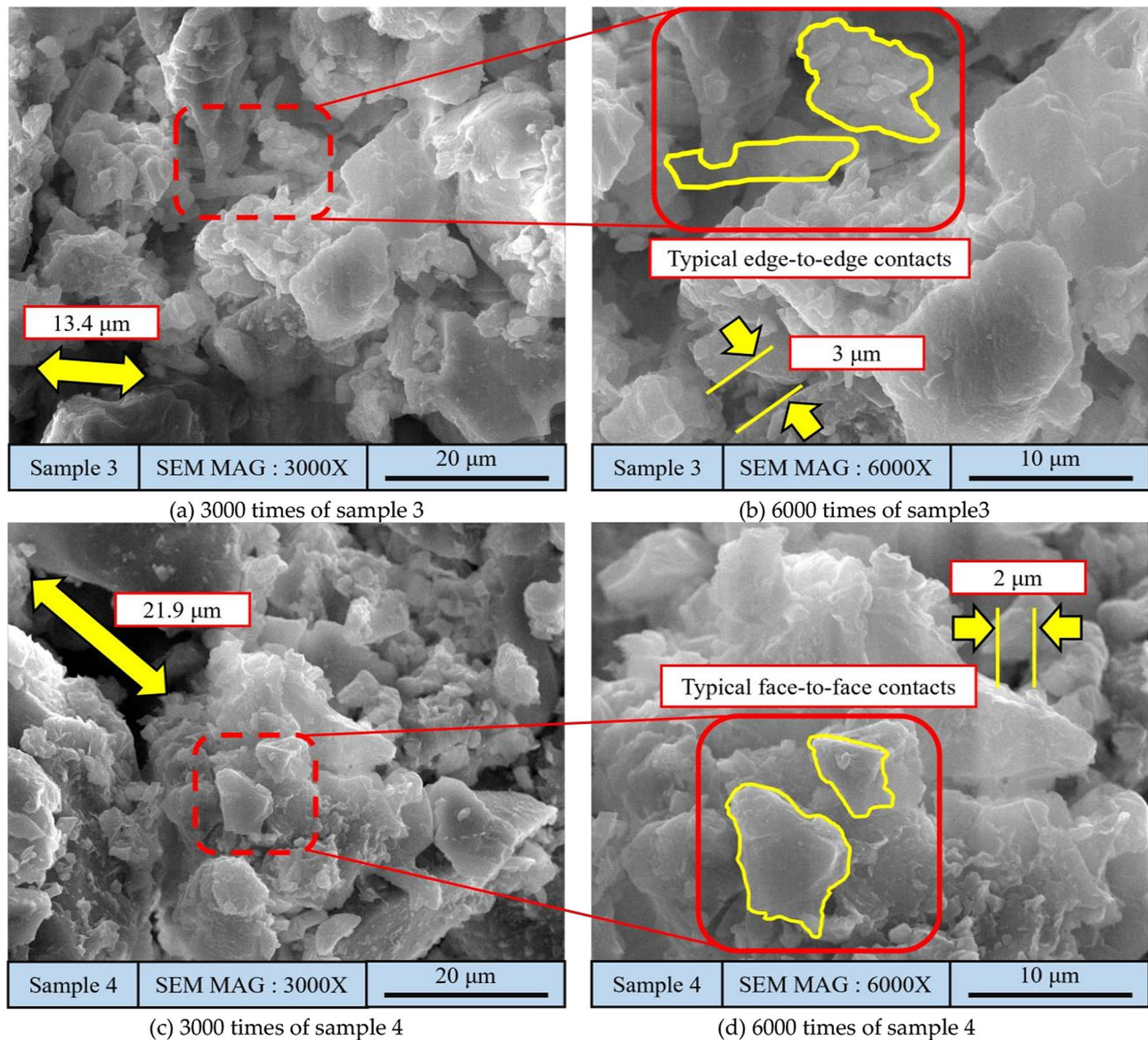


Fig. 11. The SEM images of the optimum similar material in block form.

Phase composition analysis

The phase composition of the best similar materials of PAL round gravel has been analyzed by X'pert3 X-ray powder diffraction (XRD) system (Malvern Panalytical system). Because atoms or ions inside the crystal are arranged in a regular pattern, X-rays are scattered as they pass through the crystal. Scattered X-rays at specific angles will intensify interference and create a series of diffraction peaks that reflect the arrangement of atoms inside the crystal and appear as unique diffraction patterns. The examination of the diffraction pattern shows that most of the low and medium intensity diffraction peaks are wide or clustered, while the high and medium intensity diffraction peaks are narrow and sharp. In order to accurately identify mineral phases, peak searching is carried out for the diffraction patterns of round gravel and similar soil materials. Jade software is used to identify peaks in the diffraction patterns of round gravel and similar materials collected in the field, and then the 2θ and d values of these wide scattered or multi-peak compact middle and low diffraction peaks are accurately obtained to determine their phase^{41,42}. Figure 12 shows the phase of the round gravel and the best similar material determined by XRD pattern.

Five phases in the PAL round gravel sample can be clearly interpreted from the peak shapes in Fig. 12: quartz, mica, kaolinite, potassium feldspar (K-feldspar), and chlorite. The main mineral mass fractions are quartz 62%, mica 11.8%, kaolinite 3.1%, potassium feldspar 8% and chlorite 14.9%. While other diffraction peaks on the diffraction pattern, regardless of their intensity, exhibit small deviations from the standard characteristic peak position of the suspected mineral and their relative peak height variation regularity, Six phases can be clearly interpreted for the optimum similar material specimen: barite, dolomite, gypsum, mica, calcium silicate, and quartz. The main minerals were barite 5.7%, dolomite 67.7%, gypsum 2.4%, mica 18.9%, calcium silicate 4.9%

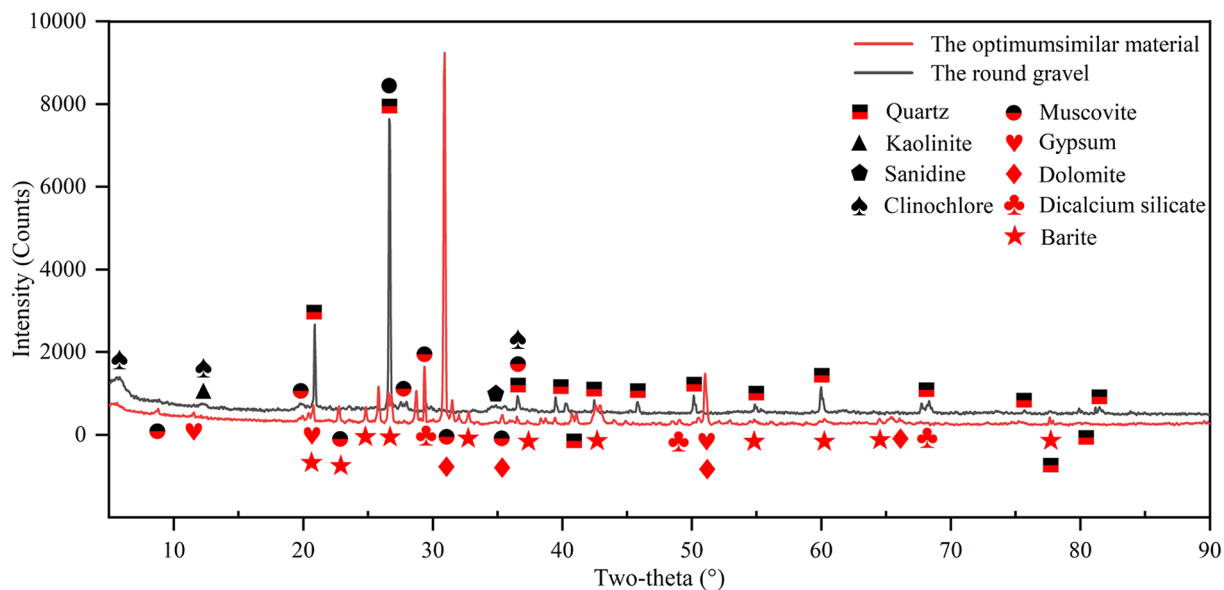


Fig. 12. Phases of the round gravel and the optimum similar material identified from the XRD patterns.

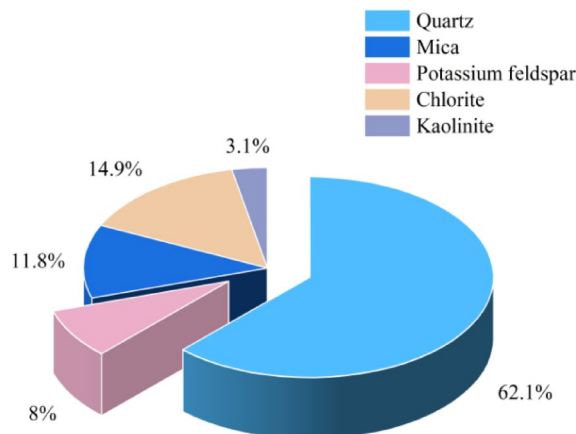


Fig. 13. The XRD quantitative phase analysis results for the round gravel collected from the field.

and quartz 0.3%. However, because the similar material was a mixture of multiple raw materials, phases with a mass fraction less than 0.1% were excluded from quantitative analysis.

XRD quantitative analysis of material phases involves the calculation of their relative percentages using the K-value method based on their diffraction characteristics and qualitative analysis of various phases. Figures 13 and 14 show the XRD quantitative phase analysis results for the round gravel collected from the field and the optimum similar material.

The hardness of mineral phases is generally expressed using the Mohs scale. The field round gravel and optimum similar material were compared in terms of their Mohs hardness based on the phase composition analysis results. The combined mass fraction of chlorite and muscovite in the round gravel was 26.7%, whereas the mass fraction of muscovite in the optimum similar material was 18.9%. Chlorite and muscovite have a hardness of 2–2.3 and 2.5–4, respectively. As muscovite is a mineral associated with chlorite, these two minerals are extremely similar in nature. The combined mass fraction of QS and K-feldspar in the round gravel was 70%. QS and K-feldspar have a hardness of 7 and 6, respectively. However, dolomite (mass fraction: 67.7%) in the optimum similar material has a hardness ranging from 3.5 to 4. In other words, the hardness of 67.7% of the phases of soil similar materials is 2–3.5 less than that of 70% of the phases of round gravel soil. Based on the above OT results, it is preliminarily concluded that using DS instead of traditional QS as the raw material for similar soil materials can effectively reduce mechanical parameters and approach ideal similar materials.

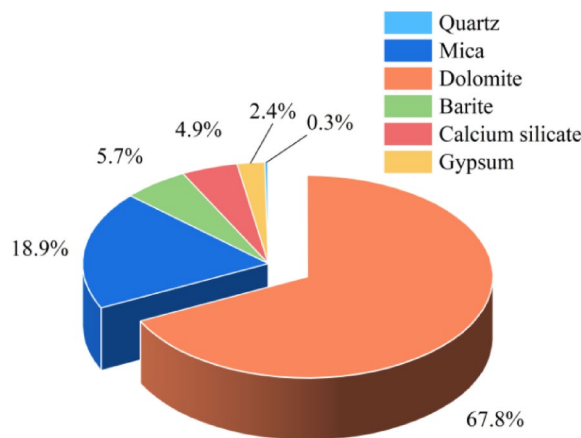


Fig. 14. The XRD quantitative phase analysis results for the optimum similar material.

3D physical model test of the ultradeep FP in PAL strata

Ultradeep FP excavation plan

The 3D physical model test system for the ultradeep FP encompassed a model box device, a data acquisition system, and an observation system. The model box device included a main steel frame, an I-beam base, a Plexiglas panel, and stiffening ribs. The data acquisition system contained pressure sensors, static strain gauges, and a computer equipped with data acquisition software. The model excavation process was observed continuously using a camcorder.

The model box device was filled with the PAL round gravel and its optimum similar material. A total of 292.83 kg of the optimum similar material was used to fill a volume of 60 cm × 50 cm × 44 cm. The model box device was filled using a layered compaction process. The maximum height of each filling layer did not exceed 5 cm. Soil pressure sensors were buried at corresponding locations. A slurry wall was also prefabricated. Figure 15 shows the 3D physical model test system for the ultradeep FP.

To allow the 3D physical model test of the ultradeep FP meet the geometric and material similarity criteria prescribed in similarity theory to further conform to the physical-process similarity criterion, the field FP construction process should be maximally followed to excavate the model. Specifically, the model should be excavated layer by layer, and internal supports should be constructed when reaching predetermined depths. The overall excavation plan consisted of six stages involving a total of 20 steps for constructing five internal supports. The net depth of excavation at each step mainly ranged from 1.5 to 2 cm. Pressure data were collected after the completion of each excavation step. The design depths of the five internal supports relative to the ground surface were -6, -14, -19, -24, and -29 cm.

Monitoring plan design

To investigate the stress-field response patterns in the surrounding soil during the excavation of the ultradeep FP of the influent pump station, 12 pressure sensors were used in the 3D physical model test^{43,44}. The stress field in this rectangular ultra-deep pit was assumed to be symmetric and the sensors were arranged hierarchically on the north, west and bottom sides of the pit model. Specifically, five pressure sensors were placed at three levels on each of the north and west center lines of the FP. The other two sensors were placed at two levels on the center vertical line of the bottom of the FP. To improve the accuracy and efficiency of monitoring data, measurement points (MPs) were spaced 3 cm apart, while the slurry wall and the bottom of the FP were set at a distance of 3 cm from the nearest MP. Two profiles were produced in the schematic diagram of the physical model of the ultradeep FP, on which the positions of the pressure sensors were marked to distinctly reveal the spatial relationship between the model elements. Figures 16 and 17 show schematic diagrams of the physical model of the ultradeep FP and the pressure sensor arrangement, respectively.

Stress-field response patterns

The excavation of the physical model of the ultradeep FP in PAL round gravel strata disturbed the original stress equilibrium in the surrounding soil, resulting in a redistribution of the stress field within a certain range^{45,46}. To understand how this stress redistribution manifests in real-time monitoring, we need to focus on the changes in stress at the monitoring points (MPs) during the excavation process. As the excavation of ultradeep FP progressed and the internal supports began to provide support, the stress at each nearby MP exhibited a clear variation pattern. The pressure at each MP was negative and decreased. The pressure at the MPs on the west and north sides was released horizontally to the FP, whereas the pressure at the bottom MPs was released upward. These distinct pressure-release patterns are crucial for understanding the overall stress-state changes during the excavation. Fig. 18 shows photographs of the excavated ultradeep FP.

Figure 19 shows the response pattern of the stress field on the west side of the FP. A pressure of 0.69 kPa was released at MP W-1, constituting the maximum pressure in the stress field. A pressure of 0.61 kPa was released at MP W-2, which was located at a horizontal distance of 3 cm from MP W-1. The second level was 10 cm away from each of the first and third levels. A comparison of the pressures at MPs W-3 and W-4 revealed that similar

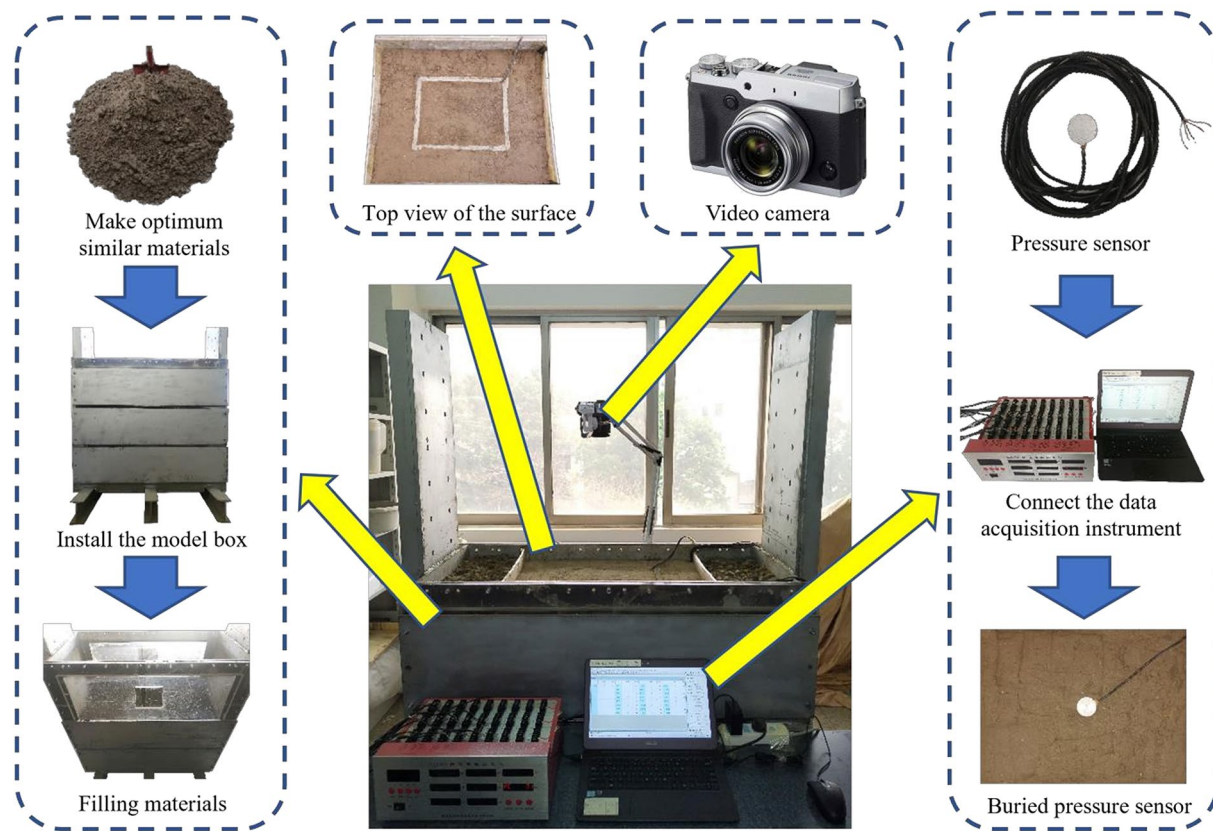


Fig. 15. The 3D physical model test system for the ultradeep FP.

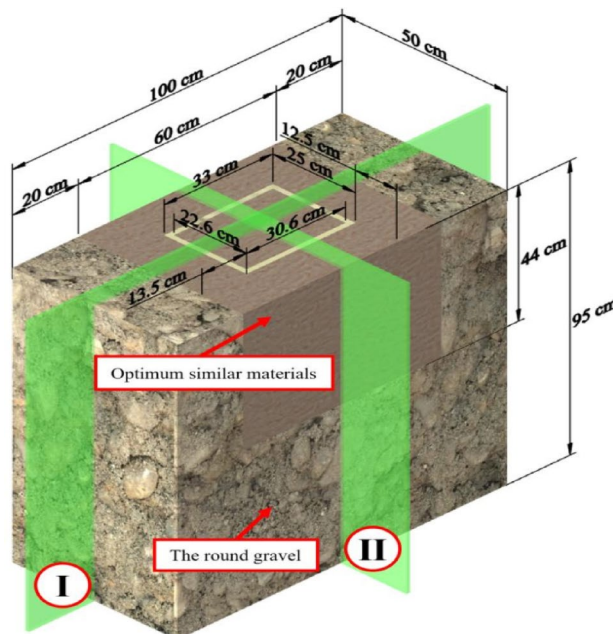


Fig. 16. Schematic diagrams of the physical model of the ultradeep FP. [Produced by WPS software with the URL <https://www.wps.cn/> and version number 12.1.0.19770].

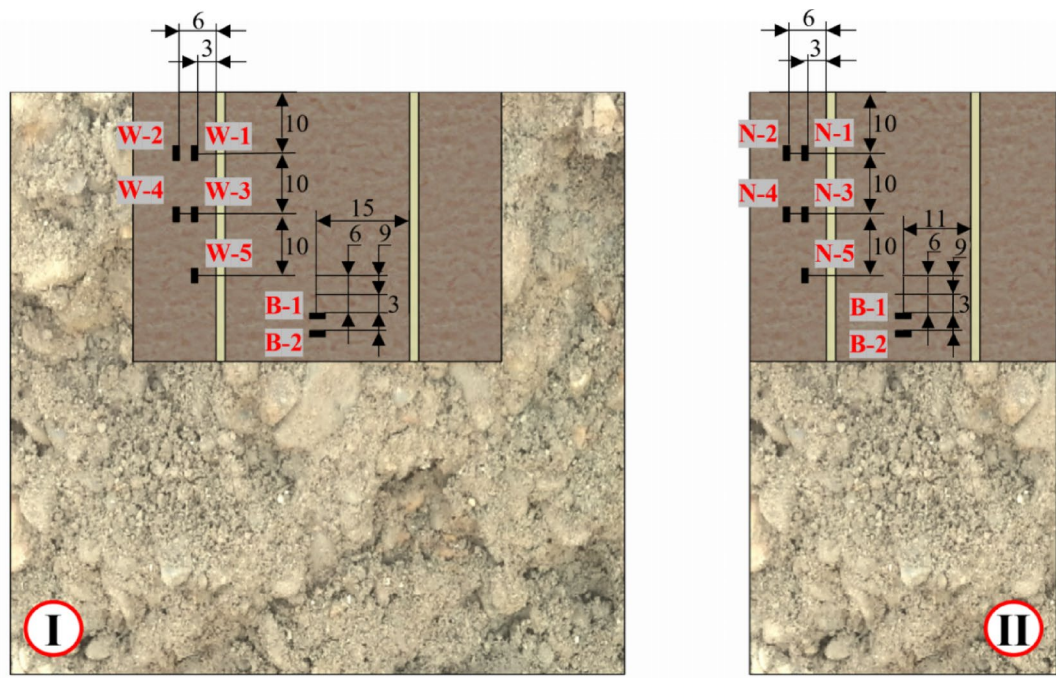


Fig. 17. Schematic diagrams of the physical model of the pressure sensor arrangement.

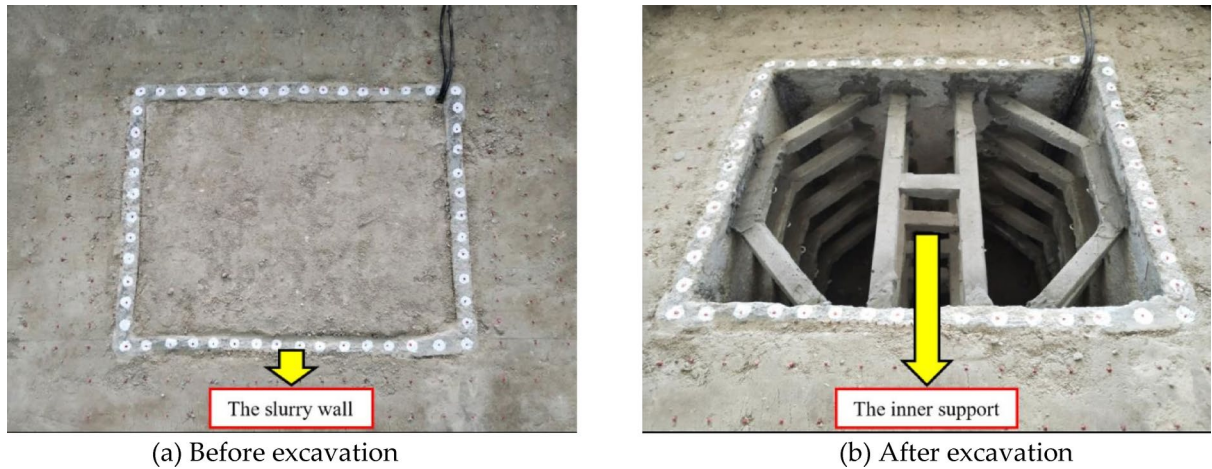


Fig. 18. Photographs of the excavated ultradeep FP.

to MPs W-1 and W-2, the pressure released at MP W-3, which was closer to the FP, was greater than that released at MP W-4. A comparison of MPs W-1, W-3, and W-5 in the vertical direction revealed that the horizontal pressure release (0.46 kPa) was the highest at MP W-1, followed by those at MPs W-3 and W-5.

Figure 20 shows the response pattern of the stress field on the north side of the FP. The irregular disturbance during the excavation process and the real-time monitoring error of the data acquisition system had the most significant impact on MP N-1, where a horizontal pressure of 0.99 kPa was released. It is noteworthy that similar pressure release trends occurred in the stress fields on the north and west sides of the FP, although the pressure release was higher on the north side than on the west side by a factor of 1–1.3. The primary cause was that the north side of the FP had a long span and a large exposed area after excavation, and that the exposed soil was significantly affected by its own weight.

Figure 21 shows the response pattern of the stress field at the center of the bottom of the FP. Most of the optimum similar material above the two MPs at the bottom of the FP was the soil excavated to construct the FP model. This material composition has a direct bearing on the stress distribution and pressure release characteristics. As a result, the vertical pressure release at each MP of the stress field at the center of the bottom of the FP considerably exceeded the horizontal pressure release from the stress fields on the north and west sides. The total vertical pressure releases at MPs B-1 and B-2 were 8.34 and 4.92 kPa, respectively. With the excavation

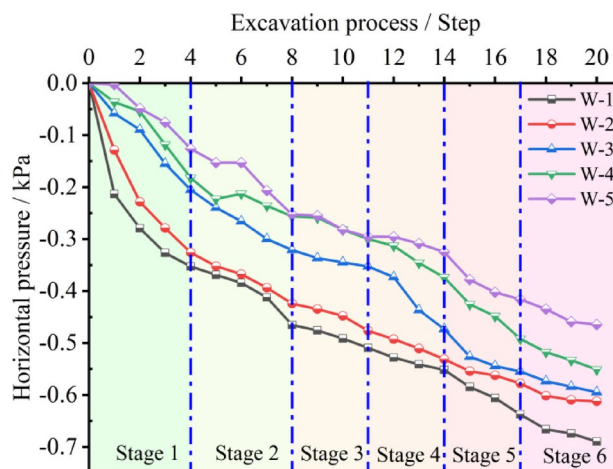


Fig. 19. Response pattern of the stress field on the west side of the FP.

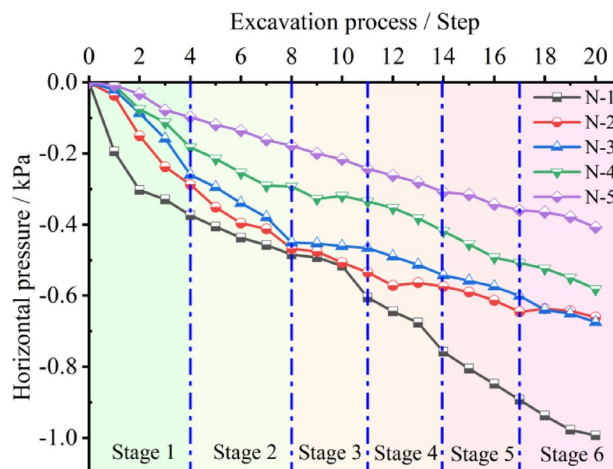


Fig. 20. Response pattern of the stress field on the north side of the FP.

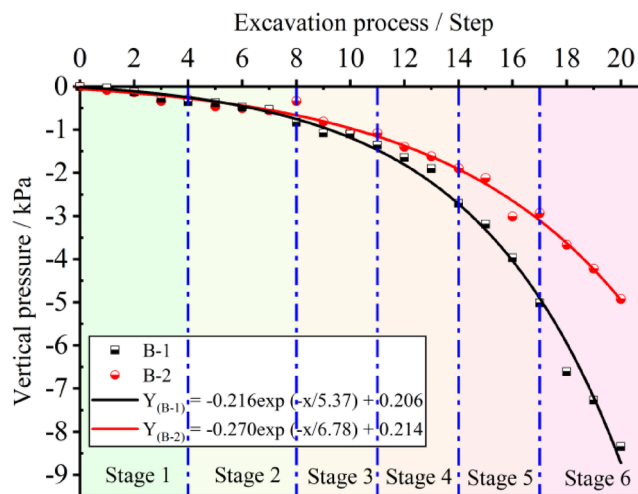


Fig. 21. Response pattern of the stress field at the center of the bottom of the FP.

of the ultradeep FP physical model and the construction of internal supports, pressure was steadily released from the stress fields on the north and west sides. However, the situation of vertical pressure release at the bottom of the FP was quite different, the vertical pressure release at the bottom of the FP increased sharply and in a nearly exponential manner:

$$Y(B-1) = -0.216 \exp(-x/5.37) + 0.206$$

$$Y(B-2) = 0.270 \exp(x/6.78) + 0.214 \quad (9)$$

The maximum pressure releases at MPs B-1 and B-2 occurred at the sixth stage, reaching 3.32 and 1.99 kPa, respectively.

Conclusion

In this study, an optimum similar material was investigated for PAL round gravel based on similarity theory and the OT design principle. After sensitivity analysis and microscopic analysis based on SEM and XRD of the similar materials, the optimum similar material was applied to a 3D physical model test of an ultradeep FP in PAL round gravel strata in order to reveal the stress-field response patterns in the soil surrounding the FP. The main conclusions are as follows:

- (1) The raw-material mix ratio for preparing an optimum similar material for PAL round gravel was determined as follows: gypsum: LD: bentonite: water: barite powder: DS = 1: 1: 1.4: 3.5: 8.8: 13.2. Analysis of the sensitivity factors of nine similar materials revealed that the LD–gypsum ratio controlled E, that the barite powder content controlled γ , and that the bentonite content controlled both c and φ .
- (2) The three main microscopic reasons of the low c and low E of the optimum similar material—nonuniform particle distribution, edge-to-face contacts and a small number of edge-to-edge contacts between particles, and small pores and a small number of large pores between particles. The combined mass fraction of QS and K-feldspar in the round gravel was 70%. The Mohs hardness of dolomite, which constituted 67.7% (mass fraction) of the optimum similar material, was lower than that of QS and K-feldspar. Therefore, using DS rather than conventional QS as a raw material can produce a similar material for the target soil with mechanical parameters closer to those of the ideal similar material.
- (3) As the excavation of the ultradeep FP progressed, the overall horizontal pressure release from the stress field was higher by a factor of 1–1.3 on the north side of the FP than on its west side. The closer the level of the MP was to the ground surface, the greater the horizontal pressure release was. However, pressure was released from the stress field at the center of the bottom of the FP at an increasing rate and in a nearly exponential manner. The maximum pressure releases at MPs B-1 and B-2 occurred at the sixth stage, reaching 3.32 and 1.99 kPa, respectively. The successful implementation of the 3D physical model test of the ultradeep FP demonstrated that the optimum similar material for PAL round gravel fully meets the test requirements for mechanical properties.

Data availability

All relevant data are within the paper.

Received: 19 September 2024; Accepted: 18 April 2025

Published online: 13 May 2025

References

1. Qiang, X. D. et al. Research on countermeasures for the construction and development of transportation underground space system. *Chin. J. Geotech. Eng.* **46**(S2), 130–134.1 (2024).
2. Sai, C. & Bai, J. Underground space: Resources to be developed Beijing Society of Mechanical Engineering. In *Proceedings of the 30th Annual Conference of Beijing Force Society*. China University of Mining and Technology (Beijing), 524–526 (2024).
3. Peng, F. L. et al. A collaborative approach for urban underground space development toward sustainable development goals: Critical dimensions and future directions. *Front. Struct. Civ. Eng.* **15**, 20–45 (2021).
4. Xiaoxue, Li. et al. Study on coupling effect of risk Factors in urban underground space construction. *J. Civ. Eng.* **54**(S1), 76–86 (2021).
5. Chi, Z. & Deng, M. Progressive failure mechanism of existing-supplementary double-layer piles retaining excavation beneath existing underground space. *Sci. Rep.* **14**, 24357 (2024).
6. Otake, Y. & Honjo, Y. Challenges in geotechnical design revealed by reliability assessment: Review and future perspectives. *Soils Found* **62**, 101129 (2022).
7. Zhang, Z., Gao, Y., Zheng, X., Cao, J. & Chen, Y. Development and application of similar materials for foundation pit excavation model test of metro station. *Appl. Sci.* **12**(24), 12880 (2022).
8. Jiahua, M. et al. Research on centrifugal model test design of shield tunnel structure response under excavation of foundation pit and precipitation. *J. Civ. Eng.* **57**(S1), 184–189 (2024).
9. Xin-Yu, Z. et al. Experimental study on the ratio of ultra-high strength similar materials for large similarity ratio model test. *Coal Geol. Explor.* **51**(11), 109–118 (2023).
10. Zhan, X. et al. Experimental study on proportioning of ultra-high strength similar materials for large similarity ratio model tests. *Coal Geol. Explor.* **51**(11), 109–118 (2023).
11. Guo, Y. H., Kong, Z. J., He, J. & Yan, M. Development and application of the 3D model test system for water and mud inrush of water-rich fault fracture zone in deep tunnels. *Math. Probl. Eng.* **2021**, 8549094 (2021).
12. Hang, Li. et al. Unloading aging of multi-step excavation of soft soil foundation pit and its influence on adjacent tunnel. *J. Central South Univ. (Nat. Sci. Ed.)* **54**(03), 1044–1053 (2023).
13. Peng, X. et al. Study on strength characteristics and mix ratio of transparent similar materials in tunnel surrounding rock. *J. Human Univ. (Nat. Sci. Ed.)* **52**(01), 219–227 (2019).

14. Zhou, W. Z. Study on selection of similar materials and physical model experiment in karst pile foundation model experiment. *Hebei University of Technology* (2020).
15. Yonghua, S., Bin, C., Biao, L. et al. Model test of similar materials for static cracks in non-circular holes. *J. Railw. Sci. nd Eng.* 1–10 (2025).
16. Jongpradist, P. et al. High internal pressure induced fracture patterns in rock masses surrounding caverns: Experimental study using physical model tests. *Eng. Geol.* **197**, 158–171 (2015).
17. Wang, B. et al. Experimental study on the mechanism of rockburst in tunnel construction by drilling and blasting construction in high ground stress stratum. *Sci. Rep.* **15**, 8914 (2025).
18. Miao, Y. B., Wei, W., Chen, R. C. & Lv, L. X. Orthogonal experiment on the mixture ratio of soil similar material. *J. Fuzhou Univ. Nat. Sci. Ed.* **44**(4), 570–576 (2016).
19. Dou, Y. M., Wang, J. N., Tian, G. Z. & Wei, M. Research on proportioning of soft soil similar materials based on orthogonal experiment. *J. Railw. Sc. Eng.* **14**(03), 480–487 (2017).
20. Wang, X. R. et al. Experimental research of the AE responses and fracture evolution characteristics for sand-paraffin similar material. *Constr. Build. Mater.* **132**, 446–456 (2017).
21. Wang, J. N., Dou, Y. M., Li, B. C., Zhu, X. X. & Li, J. W. Experimental study on effect of raw material component on mechanic property of similar soil material. *Water Resour. Hydro Eng.* **49**(8), 177–185 (2018).
22. Chu, Z. F. et al. Research on rheological similar material of soft rock based on Burgers model. *Chin. J. Rock Mech. Eng.* **237**(05), 1185–1198 (2018).
23. Fu, H. Y., Qi, S. X., Shi, Z. N. & Zeng, L. Mixing ratios and cementing mechanism of similar silty mudstone materials for model tests. *Adv. Civ. Eng. Mater.* **2021**, 2426130 (2021).
24. Yang, M. Z., Yang, Y., Zhao, B. & Nascimbene, R. Study on the proportion of conglomerate similar materials based on the orthogonal test. *Shock Vib.* **2021**, 6657323 (2021).
25. Xu, Z. L. et al. Mechanical properties and reasonable proportioning of similar materials in physical model test of tunnel lining cracking. *Constr. Build. Mater.* **300**, 123960 (2021).
26. Guo, Y. H., Yang, Y., Kong, Z. J. & He, J. Development of similar materials for liquid-solid coupling and its application in water outburst and mud outburst model test of deep tunnel. *Geofluids* **2022**, 8784398 (2022).
27. Zhang, Z., Gao, Y., Zheng, X., Cao, J. & Chen, Y. Development and application of similar materials for foundation pit excavation model test of metro station. *Appl. Sci.* **12**, 12880 (2022).
28. Dou, B. Y., Zhang, J. P., Yang, Y. C. & Niu, X. C. Study on soil deformation parameters around deep pit by large-scale physical model test. *J. Basic Sci. Eng.* **27**(01), 216–225 (2019).
29. Mu, H. D., Deng, Y. H., Zhang, W. D. & Song, D. Y. Model tests on deformation characteristics of foundation pit at Luoyang Railway Station. *Chin. J. Geotech. Eng.* **43**(S1), 198–203 (2021).
30. Fengshan, M., Jie, G. et al. Experimental research on the ratio of similar materials in large-scale engineering model Test. *J. Northeastern Univ. (Nat. Sci. Ed.)*, **20**, 41(11):1653–1660.
31. Cailong, A., Liangqing, W., Jianlin, T. et al. Development and application of solid-liquid two-phase similar materials for model test of reservoir rock slope. *Earth Sci.* 1–20 (2025).
32. Yufei, G., Zhu, C. & Zhu, G. Analysis of physical properties of similar materials in coal and rock based on mine physical model. *Appl. Geophys.* **20**(01), 116–129+132 (2023).
33. Minghe, Ju. et al. Study on impact tendency of coal in physical similarity simulation of rock burst. *Chin. J. Rock Mech. Eng.* **43**(12), 2940–2955 (2019).
34. Hongru, W., Mi, Z., Zilan, Z. et al. Study on similar materials in quasi-static scaling test of cross-fault tunnel. *Eng. Mech.* **202**, 39(06), 21–30+145.
35. Yu, Y. F., Wang, P., Wang, H. J., Xu, S. Y. & Guo, H. T. Physical model test of seismic dynamic response to accumulative landslide. *Rock Soil Mech.* **40**(S1), 172–180 (2019).
36. Xiaojing, L. et al. Analysis and numerical simulation of efficiency factors of TBM rock breaking in deep rock mass based on orthogonal design. *J. Central South Univ.* **29**(04), 1345–1362 (2022).
37. Liu, X. M., Sheng, Q., Chen, J., Ke, W. H. & Yang, J. H. Seis-mic shaking table test for large scale underground cavern (2015).
38. Chunpeng, S. et al. Orthogonal test of compressive strength of similar materials and influence coefficient of material strength. *Mater. Rev.* **37**(23), 64–69 (2023).
39. Xin, Z. et al. Applications of scanning electron microscopy in polymer characterization. *Acta Polym. Sin.* **53**(05), 539–560 (2022).
40. Kieverts, A. J. et al. Optical STEM detection for scanning electron microscopy. *Ultramicroscopy* **256**, 113877 (2024).
41. Li, M. et al. X-Ray Crystal diffraction spectrometer: Theory and application. *Acta Opt. Sin.* **42**(11), 1134008 (2022).
42. Das, D., Mishra, B. & Gupta, N. Understanding the influence of petrographic parameters on strength of differently sized shale specimens using XRD and SEM. *Int. J. Min. Sci. Technol.* **31**(5), 953–961 (2021).
43. Xianfeng, Ma. et al. Centrifuge simulation test study on excavation effect of spaced foundation pit. *Chin. J. Geotech. Eng.* **44**(S2), 92–96 (2022).
44. Zhao, Y. S., Cheng, Z. Q., Gao, Y. T., Wu, S. C. & Chen, C. C. Review of geomechanical similar-material test systems. *Arab. J. Geosci.* **13**(18), 906 (2020).
45. Bian, X. et al. Protective effect of partition excavations of a large-deep foundation pit on adjacent tunnels in soft soils: A case study. *Bull. Eng. Geol. Environ.* **80**, 5693–5707 (2021).
46. Shi, X. et al. Stability analysis of deep foundation pit with a double-row cast-in-place piles and diagonal steel lattice braces under sloped excavation conditions. *Sci. Rep.* **14**, 22761 (2024).

Author contributions

Author contributions: Conceptualization, Y.G.; methodology, Y.G.; software, Y.G., X.R., S.L., X.F., G.Y., G.Z., Y.Y., Z.Y., X.W and M.N.; validation, Y.G., X.R. and S.L.; formal analysis, Y.G., X.R., S.L., X.F., G.Y., G.Z., Y.Y., Z.Y., X.W and M.N.; investigation, Y.G., X.R., S.L., X.F., G.Y., G.Z., Y.Y., Z.Y., X.W and M.N.; resources, Y.G., X.R., S.L., X.F., G.Y., G.Z., Y.Y., Z.Y., X.W and M.N.; writing—original draft preparation, Y.G. X.R. and L.S.; writing—review and editing, Y.G., X.R., S.L., X.F., G.Y., G.Z., Y.Y., Z.Y., X.W and M.N.; funding acquisition, Y.G. All authors have read and agreed to the published version of the manuscript.

Funding

This study was supported by Key Project of Yunnan Fundamental Research Projects (no. 202501AS070107); General projects of Yunnan Fundamental Research Projects (202301AT070454), Special Project for Young Talents of Yunnan Province's Xingdian Talent Support Program (KKXX202467043), The talent training fund of Kunming University of Science and Technology (KKZ3202367014), National Innovation and Entrepreneurship Training Project for College Student of China (2021106740085) and (2021106740086), B-level Science and Technology Plan Project of Yunnan Construction Investment Holding Group Co.,Ltd (2024DJR005).

Declarations

Competing interests

The authors declare no competing interests.

Additional information

Correspondence and requests for materials should be addressed to Y.G.

Reprints and permissions information is available at www.nature.com/reprints.

Publisher's note Springer Nature remains neutral with regard to jurisdictional claims in published maps and institutional affiliations.

Open Access This article is licensed under a Creative Commons Attribution-NonCommercial-NoDerivatives 4.0 International License, which permits any non-commercial use, sharing, distribution and reproduction in any medium or format, as long as you give appropriate credit to the original author(s) and the source, provide a link to the Creative Commons licence, and indicate if you modified the licensed material. You do not have permission under this licence to share adapted material derived from this article or parts of it. The images or other third party material in this article are included in the article's Creative Commons licence, unless indicated otherwise in a credit line to the material. If material is not included in the article's Creative Commons licence and your intended use is not permitted by statutory regulation or exceeds the permitted use, you will need to obtain permission directly from the copyright holder. To view a copy of this licence, visit <http://creativecommons.org/licenses/by-nc-nd/4.0/>.

© The Author(s) 2025